

PAIR-INSTABILITY SUPERNOVAE IN THE LOCAL UNIVERSE

DANIEL J. WHALEN^{1,2}, WESLEY EVEN³, JOSEPH SMIDT¹, ALEXANDER HEGER⁴, RAPHAEL HIRSCHI^{5,6}, NORHASLIZA YUSOF⁷,
MASSIMO STIAVELLI⁸, CHRIS L. FRYER³, KE-JUNG CHEN⁹, AND CANDACE C. JOGGERST¹⁰*Draft version June 7, 2019*

ABSTRACT

The discovery of 150 - 300 M_{\odot} stars in the Local Group and pair-instability supernova candidates at low redshifts has excited interest in this exotic explosion mechanism and poses serious challenges to current theories of galactic star formation. Realistic light curves for pair-instability supernovae at near-solar metallicities are key to identifying and properly interpreting these events as more are found. We have modeled the evolution and explosions of $Z \sim 0.1 - 0.4 Z_{\odot}$ pair-instability supernova progenitors. These stars must be 150 - 500 M_{\odot} at birth because they lose up to 80% of their mass to strong line-driven winds and explode as bare He cores. Their light curves and spectra are quite different from those of Population III pair-instability explosions, which therefore cannot be used as templates for low-redshift events. Our numerical models show that non-zero metallicity pair-instability supernovae are generally dimmer than Population III explosions but can still be detected at $z \sim 0.1 - 1$ by the new supernova factories. They also reveal that pair-instability explosions can masquerade as dim, short-duration supernovae, and that under the right conditions they could be hidden in a wide variety of supernova classes. We also report for the first time that some pair-instability explosions can create black holes with masses of $\sim 100 M_{\odot}$.

Subject headings: early universe – galaxies: high-redshift – stars: early-type – supernovae: general – radiative transfer – hydrodynamics – cosmology:theory – stars: Population II – supernovae: individual (SN 2007bi)

1. INTRODUCTION

The recent discovery of stars with masses above 150 M_{\odot} in the star cluster R136 (Crowther et al. 2010) and the detection of pair-instability supernova (PI SN) candidates SN 2007bi at $z = 0.123$ (Gal-Yam et al. 2009; Young et al. 2010) and SN 2213 - 1745 at $z = 2.05$ (Cooke et al. 2012) have excited interest in this exotic explosion mechanism and challenged current theories of galactic star formation. In particular, it is not understood how so massive a progenitor can form in metallicities like those of the Small Magellanic Cloud, $\sim 0.1 Z_{\odot}$. Models of Population III (Pop III) stellar evolution predict that metal-free stars must have initial masses of 140 - 260 M_{\odot} to die as PI SNe (Heger & Woosley 2002) (although Chatzopoulos & Wheeler 2012, have now extended the lower mass limit down to 85 M_{\odot} if the star

is rotating). Stars forming in $Z \sim 0.1 Z_{\odot}$ gas may have to be much more massive at birth to die as PI SNe because they can lose most of their mass over their lifetimes to line-driven winds (Schaerer 2002; Vink et al. 2001). The conundrum lies in the fact that radiative cooling in gas and dust at such metallicities would almost certainly cause it to fragment on mass scales that are an order of magnitude below those required to produce PI SNe.

Understanding the observational signatures of PI SNe at near-solar metallicities is key to identifying and properly interpreting these events, since current and future SN factories like the Palomar Transient Factory (PTF; Law et al. 2009), the Panoramic Survey Telescope & Rapid Response System (Pan-STARRS) (Kaiser et al. 2002), and the Large Synoptic Survey Telescope (LSST; Ivezić et al. 2008) may harvest large numbers of them. Until now, numerical studies have focused on Pop III PI SNe as probes of the properties of the first stars (Bromm et al. 2003; Scannapieco et al. 2005; Kitayama & Yoshida 2005; Whalen et al. 2008b; Fryer et al. 2010; Kasen et al. 2011; de Souza et al. 2011; Vasiliev et al. 2012; Pan et al. 2012a,b; Meiksin & Whalen 2013; Whalen et al. 2013a,d; de Souza et al. 2013) (see also Whalen et al. 2013b,c,e; Johnson et al. 2013b; Whalen et al. 2013f,g). The goal of these studies was also to better understand primeval galaxies and the origin of supermassive black holes (e.g., Whalen & Fryer 2012) (see Whalen 2012; Glover 2013, for recent reviews).

But to understand PI SNe in the local universe, one must begin with non-zero metallicity progenitors for two reasons. First, metals substantially alter the internal structure of massive stars and can lead to heavy mass loss. Mass loss in turn can shorten the duration of SN

¹ T-2, Los Alamos National Laboratory, Los Alamos, NM 87545

² Universität Heidelberg, Zentrum für Astronomie, Institut für Theoretische Astrophysik, Albert-Ueberle-Str. 2, 69120 Heidelberg, Germany

³ CCS-2, Los Alamos National Laboratory, Los Alamos, NM 87545

⁴ Monash Centre for Astrophysics, Monash University, Victoria, 3800, Australia

⁵ Astrophysics Group, EPSAM, University of Keele, Lennard-Jones Labs, Keele, ST5 5BG, UK

⁶ Institute for the Physics and Mathematics of the Universe, University of Tokyo, 5-1-5 Kashiwanoha, Kashiwa 277-8583, Japan

⁷ Department of Physics, University of Malaysia, 50603 Kuala Lumpur, Malaysia

⁸ Space Telescope Science Institute, 3700 San Martin Drive, Baltimore, MD 21218

⁹ Department of Astronomy and Astrophysics, UCSC, Santa Cruz, CA 95064

¹⁰ XTD-3, Los Alamos National Laboratory, Los Alamos, NM 87545

light curves (LCs) by reducing the mass of ^{56}Ni formed in the explosion and radiation diffusion timescales in the ejecta (Kasen et al. 2011):

$$t_d \sim \kappa^{\frac{1}{2}} M_{\text{ej}}^{\frac{3}{4}} E^{-\frac{3}{4}}. \quad (1)$$

Second, Pop III stars explode in low-density relic H II regions (Whalen et al. 2004; Kitayama et al. 2004; Alvarez et al. 2006; Abel et al. 2007; Wise & Abel 2008; Whalen & Norman 2008a,b) while PI SNe in the local universe may occur in heavy winds and bubbles blown by the star. Dense envelopes can have large effects on the light curves of SNe, either quenching them or brightening them. For example, outbursts prior to the death of the star can eject massive shells with which the SN later collides, producing an event that is far more luminous than the explosion itself. The effects of higher metallicity on radiation flow in the ejecta and surrounding interstellar medium (ISM) are also unknown. They could be important, since variations in opacity of just a factor of 3 or 4 can lead to fluctuations in optical depth and luminosity by factors of 50 or more.

We have now modeled the PI SN explosions of very massive $Z \sim 0.1 - 0.4 Z_{\odot}$ stars and calculated their light curves and spectra. In Section 2 we discuss our stellar evolution and SN models, how the SNe were subsequently evolved, and how spectra were obtained from their blast profiles. We study explosions in dense envelopes in Section 3 and explosions in diffuse environments in Section 4. Fallback and black hole formation are examined in Section 5, and we conclude in Section 6.

2. NUMERICAL ALGORITHM

We compute light curves and spectra in four stages. First, 150 - 500 M_{\odot} stars are evolved from the beginning of the main sequence to the end of He burning and onset of the PI in the GENEVA code. We then explode the star in the Kepler code, solving for all nuclear burning and evolving the shock to just below the surface of the star. Shock breakout and expansion into the wind are then modeled with the RAGE radiation hydrodynamics code. Finally, we post process blast profiles from RAGE with the SPECTRUM code to compute spectra and construct light curves.

2.1. GENEVA Stellar Evolution Model

We evolved 150, 200, and 500 M_{\odot} stars in the latest version of the GENEVA code (Hirschi et al. 2004; Eggenberger et al. 2008). Our simulations include mass loss and stellar rotation, which are crucial to the evolution of very massive stars. We employ the theoretical prescription for mass loss from O stars of Vink et al. (2001) (which have been empirically corroborated by Mokiem et al. 2007) up to the onset of the Wolf-Rayet (WR) phase. The WR phase is taken to begin when the H mass fraction χ_H at the surface of the star falls below 5% when $T_{\text{eff}} > 10^4$ K, at which point we transition to empirical mass loss rates (Nugis & Lamers 2000). We describe our prescription for mass loss in greater detail in Yusof et al. (2013). Three of our four models are non-rotating; the fourth, a 500 M_{\odot} star, is given a rotational velocity $v_{\text{init}} = 0.4 v_{\text{crit}}$, where v_{crit} is the critical (breakup) velocity. This results in a surface equatorial velocity of ~ 450 km/s. The main effects of rotation are included in our calculations: centrifugal support,

TABLE 1
PI SN PROGENITOR MODELS (MASSES ARE IN M_{\odot})

run	M_{init}	M_{He}	E_{ex} (B)	M_{Ni}	Z (Z_{\odot})
h150	150	109	42.0	9.2	0.14
h200	200	130	65.0	39.2	0.14
h500s0	500	94	3.7	2.2	0.43
h500s4	500	76	10.4	0.18	0.43

mass-loss enhancement and especially mixing in radiative zones (Maeder 2009). The 150 and 200 M_{\odot} stars have $Z \sim 0.14 Z_{\odot}$ corresponding to those of the Small Magellanic Cloud. The two 500 M_{\odot} stars have metallicities $Z \sim 0.43 Z_{\odot}$ corresponding to those of the Large Magellanic Cloud. By the end of their evolution in GENEVA all four stars have shed their hydrogen envelopes and are essentially bare He cores.

2.2. KEPLER Burn Models

The star is evolved from the end of core He burning through explosive O and Si burning and then almost to shock breakout in the one-dimensional (1D) Kepler code (Weaver et al. 1978; Woosley et al. 2002). The explosion is the natural endpoint of stellar evolution in Kepler and is not artificially triggered. Its energy is set by how much O and Si burns, which takes ~ 20 s. We calculate energy production with a 19-isotope network up to the point of oxygen depletion in the core and with a 128-isotope quasi-equilibrium network thereafter. The number of mass zones in the models varied from 1000 - 1200 and was always sufficient to resolve the SN and surrounding star. We summarize the properties of our PI SNe in Table 1. Their explosion energies vary from 3.7 to 65 B (1 B = 10^{51} erg). The s0 and s4 designations in Table 1 refer to non-rotating and rotating stars, respectively.

2.3. RAGE Simulations

Shock breakout and expansion into the wind is modeled with the radiation hydrodynamics code RAGE (Gittings et al. 2008). Our models include multi-species advection, energy deposition by radioactive decay of ^{56}Ni , grey flux-limited diffusion with LANL OPLIB opacities¹¹ (Magee et al. 1995), and 2-temperature physics. We evolve mass fractions for the 15 even-numbered elements that are predominantly synthesized by PI SNe. Both the self-gravity of the ejecta and the gravity of any object formed at the center of the grid due to fallback are included in our simulations. Self-gravity is important at early times because the potential energy of the ejecta is close to its kinetic, internal and radiation energies. Failure to include it causes the shock to break out of the star with far higher energies and luminosities than it actually has. Point-mass gravity is important in weak explosions in which much of the star may remain gravitationally bound and later fall back on itself.

We evolve the explosions on a 1D spherical coordinate grid in RAGE. A 1D mesh is sufficient because PI SNe exhibit little of the internal mixing that would break spherical symmetry. Joggerst & Whalen (2011) recently investigated such mixing in the early stages of both blue giant

¹¹ <http://aphysics2/www.t4.lanl.gov/cgi-bin/opacity/tops.pl>

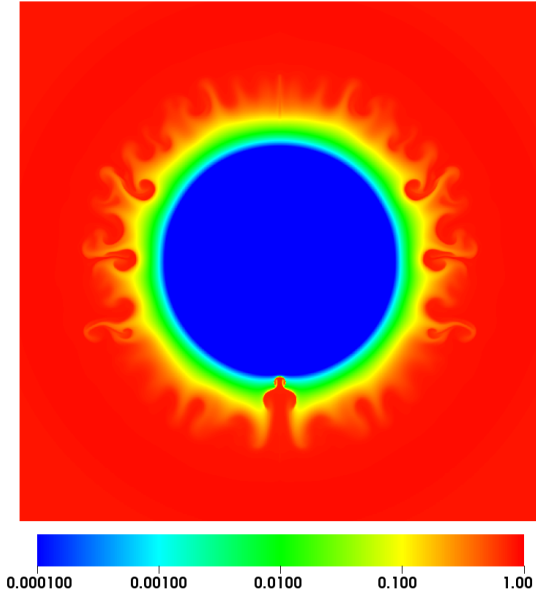


FIG. 1.— Mixing in the oxygen shell (the site of explosive burning) in the $500 M_{\odot}$ $0.1 Z_{\odot}$ PI SN; this image shows O mass fraction. Mild instabilities form during explosive burning. The shock is about to break through the surface of the He core on larger scales not shown in this image. The minor mixing found in these PI SNe introduces only minor departures from spherical symmetry, justifying the use of 1D models for their light curves.

and red supergiant Pop III PI SNe with two-dimensional (2D) simulations done with the AMR code CASTRO (Almgren et al. 2010). They found only minor mixing in two of their nine models, in contrast to core-collapse explosions in which there is rampant mixing prior to shock breakout (e.g., Fryer et al. 2007a; Joggerst et al. 2010).

Preliminary 2D CASTRO simulations of the explosions in this study show that if mixing occurs it is minimal, and mostly confined to the O shell where explosive burning begins (Fig. 1; Chen et al. 2011). This is partly due to the fact that the stars have shed their hydrogen envelopes prior to the explosion and breakout occurs from a He core, whose radius is just 1% that of the original star. Instabilities, if they form, have little time to develop before the shock reaches the surface. This may not always be the case; stellar rotation has now been shown to induce dynamical instabilities into the explosion in 2D PI SN models (Chatzopoulos et al. 2013).

The RAGE mesh has 150,000 zones and a resolution of 8.0×10^5 cm for the h150 and h200 models and 1.6 and 4.0×10^5 cm for the h500s0 and h500s4 models, respectively. Outflow conditions are imposed on both the inner and outer mesh boundaries. Because no compact objects are present in the Kepler profiles when they are ported to RAGE we set the point mass at the inner boundary to zero at the beginning of the run. Any fallback to the center of the grid is then tallied and incorporated into the point mass, whose gravity can evolve during the simulation.

We allocate 20 - 25% of the grid to the ejecta at setup. The initial radius of the shock varies with the star but is typically 50 - 80% that of the He core. Up to four levels of adaptive mesh refinement (AMR) are applied in the initial interpolation of the profiles onto the grid and then during the simulation. To speed up the run and

accommodate the expansion of the ejecta we resize the mesh by a factor of 2.5 every 10^6 time steps or when the radiation front has crossed 90% of the grid, whichever happens first. The initial time step on which the new series evolves scales roughly as the ratio of the outer radii of the new and old grids. We again apply up to 4 levels of refinement when mapping the explosion to a new grid and then throughout the run. The explosion is evolved out to 3 yr, until its luminosity has fallen below detection limits.

Radiation energy densities are not explicitly evolved in the Kepler models so we initialize them in RAGE by

$$e_{\text{rad}} = aT^4, \quad (2)$$

where $a = 7.564 \times 10^{-15}$ erg cm $^{-3}$ K $^{-4}$ is the radiation constant and T is the gas temperature. Also, since the gas energy in Kepler includes contributions by ionization states of atoms, we unambiguously construct the specific internal energy from T with

$$e_{\text{gas}} = C_V T, \quad (3)$$

where $C_V = 1.2472 \times 10^8$ erg gm $^{-1}$ K $^{-1}$ is the specific heat of the gas.

2.4. SPECTRUM

To calculate a spectrum we first sample the RAGE radiation energy density profile from the outer boundary inward to find the position of the radiation front, which we take to be where aT^4 rises above 10^{-4} erg/cm 3 . We then determine the radius of the $\tau = 40$ surface by integrating the optical depth due to Thomson scattering inward from the outer boundary ($\kappa_{Th} = 0.288$ for pristine H and He gas). This yields the greatest depth in the flow from which photons can escape because κ_{Th} is the minimum opacity that the photons would encounter.

Densities, velocities, temperatures and species mass fractions are then extracted from the RAGE profile and interpolated onto a 2D grid in r and θ in SPECTRUM (Frey et al. 2013), whose inner and outer boundaries are zero and 2.0×10^{17} cm, respectively. We allocate 800 uniform zones in log radius from the center of the grid to the $\tau = 40$ surface. The region from the $\tau = 40$ surface and the radiation front is then partitioned into 6200 uniform zones in radius. The wind between the radiation front and the outer boundary is divided into 500 uniform zones in log radius for a total of 7500 radial bins.

The data in each radial bin is mass averaged so that SPECTRUM captures any sharp features in the RAGE profile. The SPECTRUM grid is uniformly discretized into 160 bins in $\mu = \cos \theta$ from -1 to 1. Our choice of mesh ensures that regions of the flow from which photons can escape into the ISM are well resolved while those from which they cannot are only lightly sampled. Calculating spectra in this manner allows us to determine how a dense wind shrouding the star absorbs radiation from the explosion, an effect not considered in earlier studies. Light curves are constructed from 200 - 300 spectra. The spectra are usually logarithmically spaced in time from shock breakout to 3 yr.

2.5. Circumstellar Environment

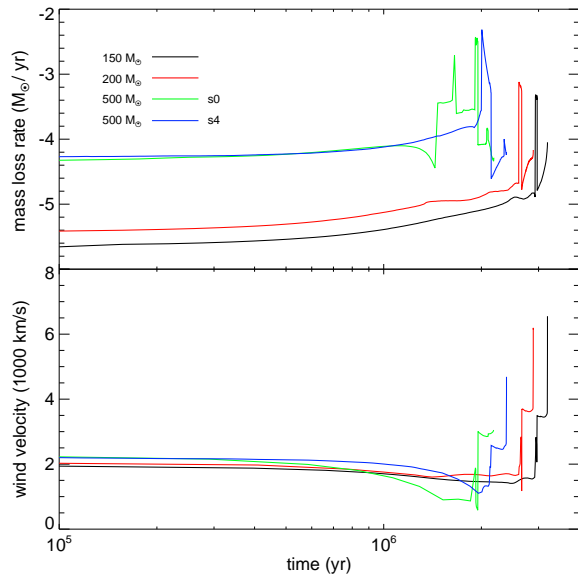


FIG. 2.— Mass loss rates \dot{m} (upper panel) and wind velocities v_w (lower panel) for the four PI SN progenitors in our study.

TABLE 2
MASS LOSS RATES AND WIND SPEEDS

$M_{\text{init}} (M_{\odot})$	$\dot{m} (M_{\odot} \text{ yr}^{-1})$	$v_w (\text{km s}^{-1})$
150	$10^{-4.8}$	3500
200	$10^{-4.8}$	3600
500s0	$10^{-4.1}$	3000
500s4	$10^{-4.4}$	2500

We show mass loss rates and wind velocities for the four progenitors in Fig. 2. The wind velocity, which is taken to be the escape velocity from the surface of the star and varies from 1000 - 6000 km s^{-1} , is time-dependent because the radius of the star, which is also a product of our stellar evolution calculations, evolves over time. The composition of the wind is primordial, 76% H and 24% He by mass. The mass loss rates and wind speeds for the stars are fairly constant for their first 1 - 2 Myr but they all exhibit strong outbursts at the end of their lives.

As shown by Mesler et al. (2012) with the ZEUS-MP code (Whalen & Norman 2006), outbursts and strong winds in principle can form quite complex structures around the star. The collision of the ejecta with such structures could strongly affect its luminosity. But the SN expands to at most ~ 0.3 pc before becoming dim so it is only the mass loss in the few years following the final outburst of each star that sets the circumstellar profile out to this radius. As shown in the bottom panel of Fig. 2, wind speeds for all four stars are relatively constant in the 10 - 100 yr after the outburst. Mass loss rates immediately after the ejections are also relatively constant over these times. The stellar envelope is therefore well-approximated by the usual power-law density

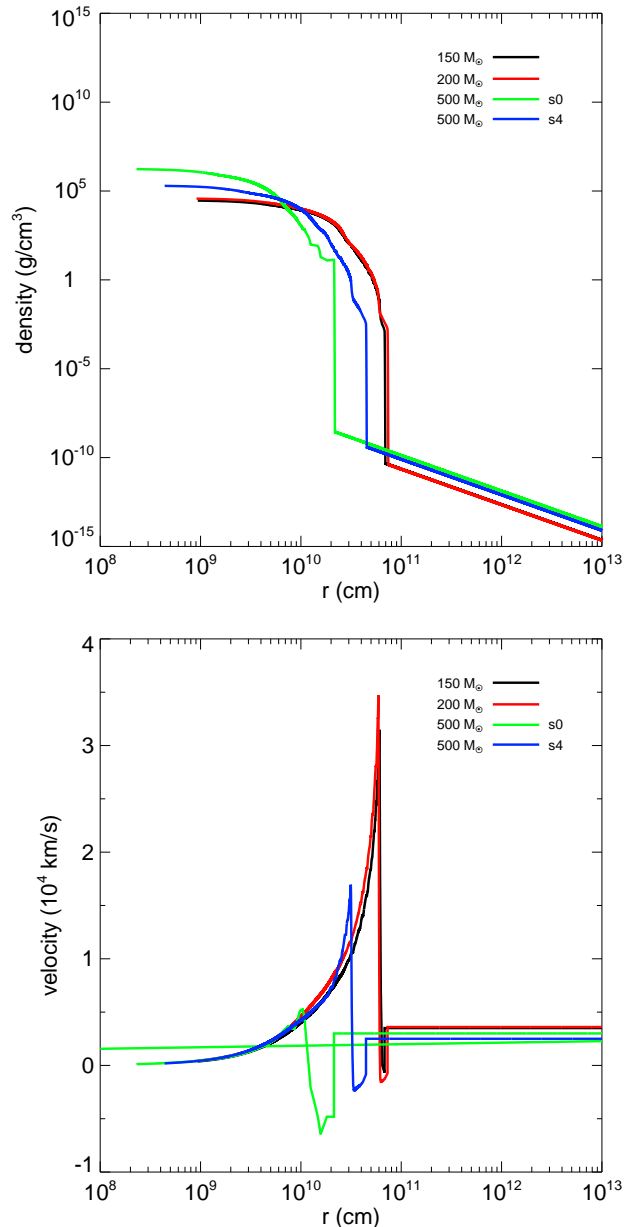


FIG. 3.— Explosion and wind profiles for all four progenitors in dense wind envelopes just before breakout from the bare He core. Top panel: densities; bottom panel: velocities. The radii of the cores vary from 10^{10} - 10^{11} cm.

profile

$$\rho = \frac{\dot{m}}{4\pi r^2 v_w}, \quad (4)$$

where v_w and \dot{m} are the wind speed and mass loss rate just after the ejection, respectively. We summarize v_w and \dot{m} in Table 2. To soften the density drop at the surface of the star (and thus prevent numerical instabilities at shock breakout) we bridge the star and the wind by an r^{-25} density profile. We show density and velocity profiles for the shock, the star, and the surrounding wind in Fig. 3.

We consider two limiting cases for the supernovae: ex-

plosions in the dense winds just described and explosions in diffuse envelopes in which the outburst clears gas from the vicinity of the star. In this latter case we use Eq. 4 for the wind with $v_w = 1000 \text{ km s}^{-1}$ and an \dot{m} chosen to guarantee that $\rho_w \sim 2 - 3 \times 10^{-18} \text{ g cm}^{-3}$ at the bottom of the density bridge from the surface of the star. We examine explosions in heavy winds first, taking the h150 PI SN as a fiducial case.

3. EXPLOSIONS IN DENSE ENVELOPES

3.1. Shock Breakout

Velocity, temperature and density plots for shock breakout from the surface of the star are shown in Fig. 4. Prior to breakout the shock is not visible to an external observer because of scattering by free electrons in the upper layers of the star. When the shock breaks through the surface of the star it abruptly accelerates in the steep density gradient there, as shown in the velocities at 0.62 s and 2.4 s. At the same time, photons that were previously trapped in the shock and simply advected along by the flow now break free of it, and a radiation pulse propagates into the wind. The radiation front is visible as the flat plateau in temperature ahead of the shock at 2.4 s and 4.1 s. The temperature of the plateau ($\sim 500 \text{ eV}$ at 2.4 s and 300 eV at 4.1 s) is the temperature to which the radiation heats the wind, not the shock itself, which is much hotter ($\sim 2 \text{ keV}$). The temperature of the plateau falls over time because the shock expands and cools and its spectral peak shifts to lower energies.

The breakout pulse is usually thought to be approximately the light crossing time of the star (here, a few seconds for the compact He core), but in reality it is somewhat longer because the photons do not instantly decouple from the shock. Instead, the pulse blows off the outermost layers of the star at very high velocities, as shown at 2.4 and 4.1 s. At 4.1 s the shock is visible in the density profile at $1.1 \times 10^{11} \text{ cm}$. The wispy outer layers of the star have been driven ahead of the shock by the radiation to $1.4 \times 10^{11} \text{ cm}$. The shock drives this radiative precursor into the wind until it cools, dims, and can no longer do so, as we show later. Radiation/matter coupling is especially strong in breakout from compact cores because the temperature of the shock is so high, twice that of breakout in the z-series PI SNe in Whalen et al. (2013f), because the shock has done less PdV work on its surroundings.

The breakout transient is composed primarily of x-rays and hard UV, and in Type Ia and II SNe its luminosity is usually $\sim 10^{42} - 10^{45} \text{ erg s}^{-1}$. The dense wind quenches most of the transient in our explosions, limiting its initial brightness to $\sim 3 \times 10^{40} \text{ erg s}^{-1}$ as shown in the left panel of Fig. 5. The flux is mostly UV and optical, with a few hard x-rays as shown in the spectrum at 2.3 s in the right panel of Fig. 5. The radiation pulse briefly ionizes part of the envelope at breakout but it rapidly recombines as the transient dies down, partially shuttering subsequent radiation from the fireball from $\sim 2 \text{ s}$ to 10^3 s as shown in the bolometric luminosity in Fig. 5. At 225 s the only emission from the fireball that escapes out through the wind is optical, IR, and some soft UV. But the luminosity again begins to rise as the shock grows in radius and more of its photons escape the wind, as shown from 10^3 to 10^5 s . As the wind beyond the shock becomes thin the UV

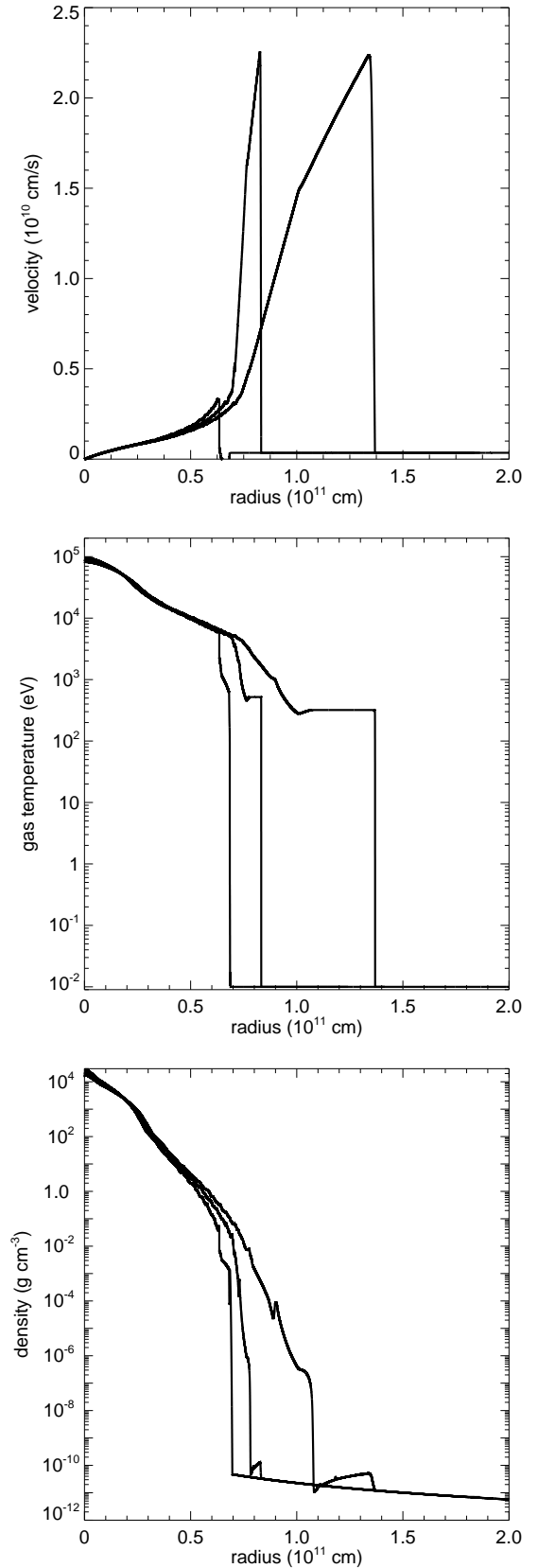


FIG. 4.— Shock breakout for the h150 PI SN in a dense envelope. Top: velocities; center: temperatures; bottom: densities. From left to right the times are 0.62 s, 2.4 s, and 4.1 s.

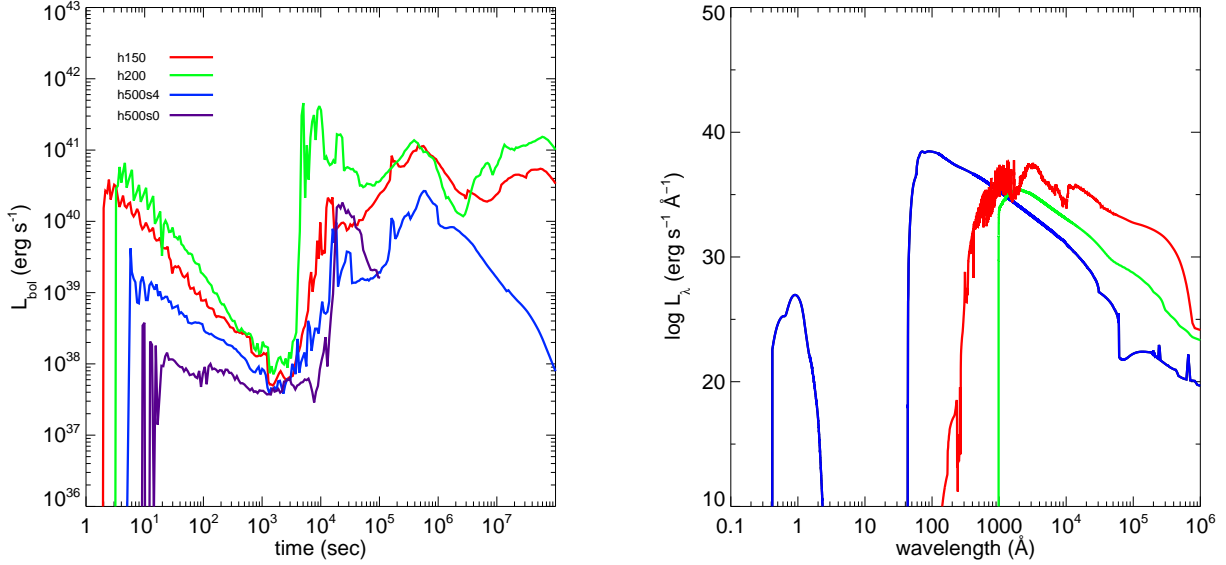


FIG. 5.— Left panel: bolometric luminosities for all 4 PI SNe in dense winds. Right panel: spectral evolution of the h150 PI SN. Blue: shock breakout from the star at 2.3 s. Green: partial quenching of the spectrum at 225 s due to recombination of the wind after being briefly ionized by the breakout pulse. Red: radiation breakout from the envelope at 1.46×10^5 s.

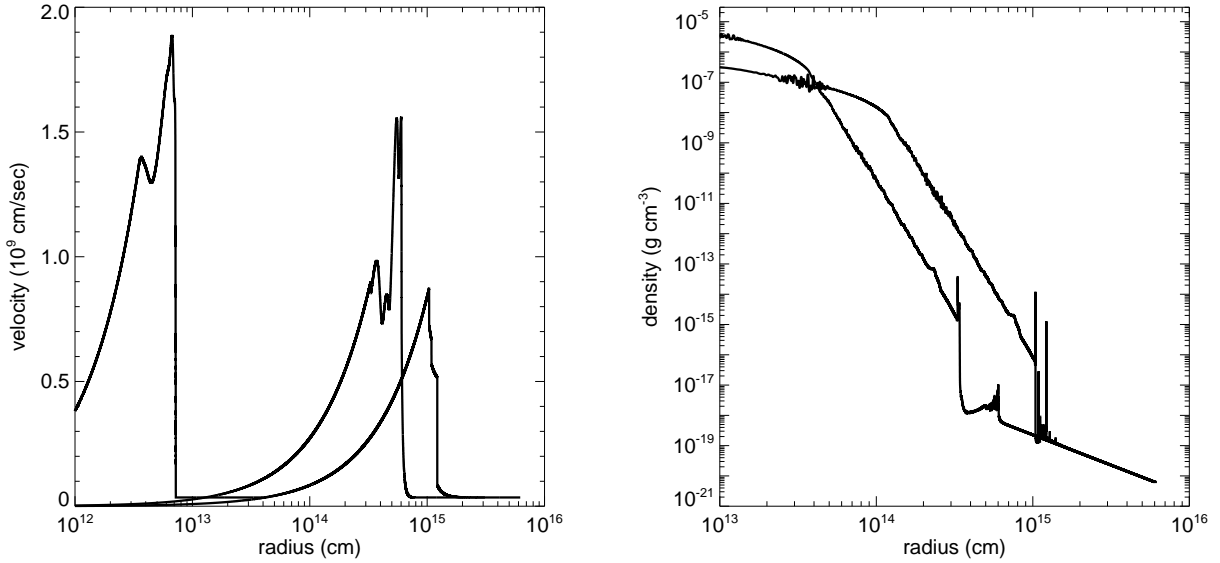


FIG. 6.— Evolution of the h150 PI SN at intermediate times. Left panel: velocities, from left to right, at 250 s, 6.8×10^4 s, and 1.2×10^5 s. Right panel: densities at 6.8×10^4 s and 1.2×10^5 s.

emission rises again, as shown in the spectrum at 1.46×10^5 s. Thus, there is a partial breakout of radiation from the envelope at shock breakout and a later, protracted rebrightening as the wind becomes optically thin to the shock.

3.2. Intermediate / Later Stages of the SN

As the SN expands it plows up the wind, but it does not immediately form a reverse shock. Instead, it continues to drive the radiative precursor ahead of it into the wind. The interface between the shock and the precursor is visible as the break in the velocity profile at 4×10^{12} cm at 250 s. There is a small density bump at the interface that oscillates in amplitude as the shock drives it forward, and this in turn causes the slight flickering

in the bolometric luminosities out to $\sim 10^3$ s. A reverse shock does form at $\sim 10^4$ s, and is visible in the velocity profile at 2.5×10^{14} cm at 6.8×10^4 s. But this shock dissipates by 10^5 s, never having propagated further back into the ejecta. At $\sim 1.5 \times 10^5$ s the forward shock overtakes and collides with the precursor at $\sim 10^{15}$ cm as shown in the density profiles, causing a small bump in the bolometric luminosity in the left panel of Fig. 5.

Soon after the precursor disappears the SN becomes a free expansion, slowing down more gradually as it encounters lower densities. The ejecta expands in a nearly self similar fashion thereafter. The light curve reaches a peak luminosity of 10^{41} erg s $^{-1}$ at 5.8 d. All four bolometric light curves exhibit similar evolution: initial par-

tial radiation breakout through the wind at shock breakout, dimming as the shock expands and cools in the wind, then a second radiation breakout and rebrightening when the shock reaches radii where the wind becomes optically thin, typically at a few 10^4 s. We also note that all four explosions brighten again at about 6 d when the photosphere abruptly drops inward to denser and hotter regions of the ejecta.

The two h500 SNe dim after just a few months while the h150 and h200 SNe are still relatively bright at 3 yr. This is due to relative ^{56}Ni production: the h500s0 and s4 explosions only make 0.18 and $2.2 M_{\odot}$ of ^{56}Ni , respectively, compared to 9.2 and $39.2 M_{\odot}$ by h150 and h200. And, as we discuss in further detail below, all the ^{56}Ni produced by h500s0 falls back into a black hole created by fallback. In comparison to Pop III PI SNe, the four h-series explosions in dense envelopes are relatively dim events. But the large ejecta mass in these SNe can still result in extended emission times due to their longer radiation diffusion timescales (Eq. 1).

The ripples in the bolometric luminosities from 10^4 - 10^5 s coincide with the appearance of the reverse shock and are likely due to the radiative instability described by Chevalier & Imamura (1982) and Imamura et al. (1984). After the reverse shock forms, it detaches from the forward shock and backsteps into the flow in the frame of the forward shock. But if the shocked gas can radiatively cool, as this gas does, the reverse shock loses pressure support and recedes back toward the forward shock. As the forward shock continues to plow up the envelope the cycle repeats. In a multidimensional simulation, the interface between the ejecta and the envelope in which the radiative instability occurs would likely be broken up by Rayleigh-Taylor (RT) instabilities, and this might reduce or remove altogether the fluctuations in the light curve over this time interval. In principle, such instabilities could also disrupt the structures emitting most of the radiation from the shock and alter the luminosity of the explosion. But given the fact that the ripples themselves have small amplitudes, it is not likely that the mean luminosity would change much in their absence.

3.3. Light Curves

We show g, r, i and z band light curves at peak brightness for the h150 explosion in Fig. 7, together with sensitivity limits for PTF, Pan-STARRS and LSST. This SN, which is typical of the models, will be visible to PTF at $z \lesssim 0.02$, to Pan-STARRS at $z \lesssim 0.1$, and to LSST at $z \lesssim 1$. We have also calculated near infrared (NIR) light curves at 1 - 4 μm for all four explosions at $z = 7, 10$ and 15. The spectra were redshifted and dimmed in the rest frame, and then convolved with absorption by the neutral IGM (Madau 1995) and filter response functions with the synthetic photometry code of Su et al. (2011). We find that all four SNe peak at \sim AB mag 35 at these three redshifts, well below the photometry limits of the *James Webb Space Telescope* (JWST) and the Wide-Field Infrared Survey Telescope (WFIRST), which are AB mag 32 and 27, respectively.

4. EXPLOSIONS IN DIFFUSE ENVELOPES

4.1. Shock Breakout

Velocity, temperature and density profiles for shock breakout in a diffuse wind are shown in Fig. 8 for the

h150 PI SN. We first note that ambient densities in this model are five orders of magnitude lower than those of the dense envelopes. The initial effect of the much lower density is that the shock heats the surrounding gas to higher temperatures after breakout, nearly 1 keV, and it remains hotter for longer times. The shock cools more rapidly in dense winds due to the PdV work it performs on its surroundings. The shock therefore has a harder spectrum when it breaks out into diffuse envelopes and, as we show later, far higher breakout luminosities because the wind at the base of the bridge is basically optically thin. In these envelopes, shock breakout and radiation breakout occur at the same time and the shock reaches peak luminosity before reaching the bottom of the bridge. Blowoff and the formation of a radiative precursor is again visible in the broken slope of the velocities near their peak at 5.12 and 6.18 s.

4.2. Early and Late Evolution

We show the early and later evolution of the h150 explosion in the left and right panels of Fig. 9. It might be thought that the break in the velocity profile at 1.25×10^{14} cm at 1.07×10^4 s is a reverse shock but it is actually due to the complete detachment of the radiative precursor from the shock that is driving it. This radiatively blown layer briefly swells to about twice the radius of the shock. There is again a bump in density slightly ahead of the shock that is visible at 7.5×10^{13} cm and 1.5×10^{14} cm at 4866 s and 1.07×10^4 s, respectively. As in our previous explosion, its amplitude fluctuates over time and causes the ripples in the bolometric luminosities out to ~ 1000 s in Fig. 10. The fluctuations here are much stronger because of the lower densities ahead of the shock. They are absent in the h500s0 light curve because it has a much lower explosion energy. As we discuss in the next section, most of the star remains gravitationally bound in this SN, and only its outer layers are blown off. There is not enough flux from the shock to drive fluctuations in the precursor.

By about 20 d the shock overtakes the radiatively-blown wind and the flow expands in a self-similar manner thereafter, as shown in the right panels in Fig. 9. The SN becomes a free expansion much earlier in the diffuse envelope. All four bolometric light curves exhibit the same rebrightening at about a week as in the previous light curves, and for the same reason: the photosphere abruptly recedes to deeper, denser and warmer regions of the flow whose structure remains unaffected by the envelope. The h150 and h200 PI SNe are brighter at late times because they produce much more ^{56}Ni than the two h500 explosions (and because the ^{56}Ni created by h500s0 falls back into a black hole, as we discuss below).

4.3. Light Curves

Because the shock breaks out into much lower densities, peak bolometric luminosities range from a few 10^{45} to 10^{46} erg s^{-1} for these explosions, about four orders of magnitude brighter than SNe in dense envelopes. But low optical depths in the surrounding envelope allow the fireball to cool more rapidly, and its lower temperatures at later times reduce its luminosity to below those in strong winds. We show g, r, i and z band light curves for the h150 PI SN in Fig. 11. They are dimmer than those

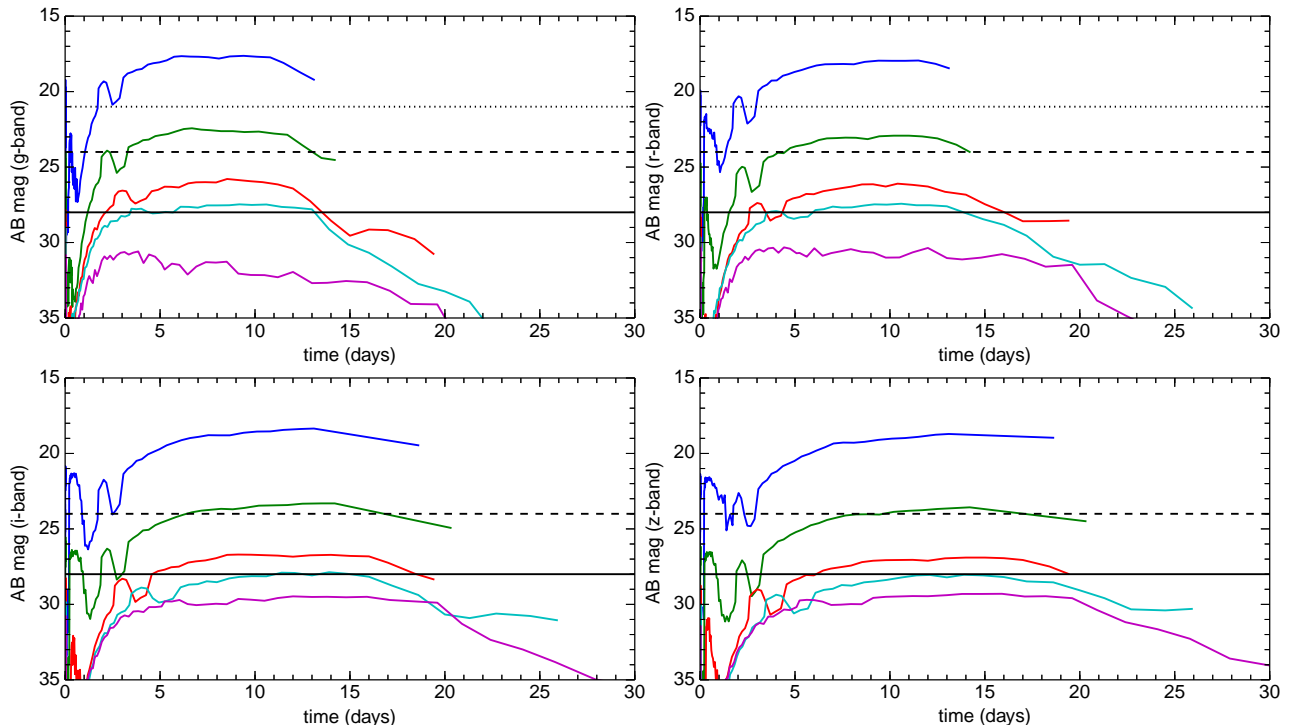


FIG. 7.— Light curves for the h150 PI SN at $z = 0.01$ (blue), $z = 0.1$ (green), $z = 0.5$ (red), $z = 1$ (teal), and $z = 2$ (purple). Dotted line: PTF detection limit; dashed line: Pan-STARRS detection limit; solid line: LSST detection limit.

for SNe in dense shrouds but last longer. In these explosions the photosphere recedes to layers that are cooler but denser that radiate for longer times because they are warmed by ^{56}Ni decay. The two h500 light curves become dim much sooner than the h150 and h200 light curves because they do not create much ^{56}Ni . These latter two SNe will be visible to LSST at low redshift.

5. FALLBACK AND BLACK HOLE PRODUCTION

PI SNe are usually thought to completely unbind the star and leave no compact remnant. Here, we report that some PI SNe do create massive black holes. In Fig. 12 we show density and velocity profiles at the center of the h500s0 explosion, which is the weakest of the set. Because this SN has a net energy of only 3.7×10^{51} erg, most of the material interior to 10^{11} cm remains gravitationally bound. At 776 s it has come to a halt, and the deepest regions begin to fall back to the center of the grid. By 785 s $\sim 30 M_{\odot}$ has fallen back to the center at peak velocities of $12,000 \text{ km s}^{-1}$ and infall rates of $\sim 15 M_{\odot} \text{ s}^{-1}$, as shown in Fig. 13. By 801 s, $\sim 90 M_{\odot}$ has collapsed to the center of the grid. In our model we neglect radiative feedback from the nascent neutron star so these infall rates should be taken to be upper limits.

Most of this material was burned to ^{56}Ni during the explosion, and it quickly forms an iron core that, as its mass grows, collapses to form a neutron star. Could this weak PI SN create the conditions for a post-outburst core-bounce SN? The fate of the infalling mass depends upon the accretion rate onto the newly formed neutron star (Fryer 1999; Fryer et al. 2012). The accretion rate determines the ram pressure that the SN engine must overcome to drive an explosion. If it is too high, the convective engine is unable to push off the accreting material, and the neutron star gains mass until it collapses

to form a black hole. For typical $15 M_{\odot}$ stars, the accretion rate during the engine phase drops below $1 M_{\odot} \text{ s}^{-1}$ in the first 100 ms. When it drops below this value, strong SN explosions are expected (Fryer 1999). In more massive stars, the accretion rate never falls below $1 M_{\odot} \text{ s}^{-1}$ (in a $25 M_{\odot}$ star it drops to just above $1 M_{\odot} \text{ s}^{-1}$ in the first second and to $2.5 M_{\odot} \text{ s}^{-1}$ in a $40 M_{\odot}$ star). These systems are usually thought to have weak or no SN explosions (Fryer 1999; Fryer et al. 2012). In our model, the accretion rate peaks at $\sim 10 M_{\odot} \text{ s}^{-1}$, so the neutron star will almost certainly collapse to a black hole without an explosion.

However, if the infalling material has enough angular momentum, this system has accretion rates that are high enough to power a standard collapsar gamma-ray burst (GRB; Popham et al. 1999). If a GRB is produced, a secondary explosion with a distinctive gamma-ray signature might accompany the PI SN. We do not expect the h500s0 model to produce a GRB because its progenitor has no rotation. By 801 s, fallback is complete, and a $90 M_{\odot}$ black hole has formed at the center of the grid.

6. CONCLUSION

It is clear that there is far more variety to PI SNe and their light curves than previously thought, and that Pop III PI SNe can no longer be considered to represent the population as a whole, particularly at higher metallicities. We find that non-zero metallicity PI SNe are dimmer than Pop III events and in general are only visible at lower redshifts. Metals lead to drastic departures from Pop III stellar evolution and final structures for the star, and they also give rise to complex circumstellar media. Because the structure of the ejecta and its surroundings can both radically alter the light curve of the explosion, PI SNe at near-solar metallicities can-

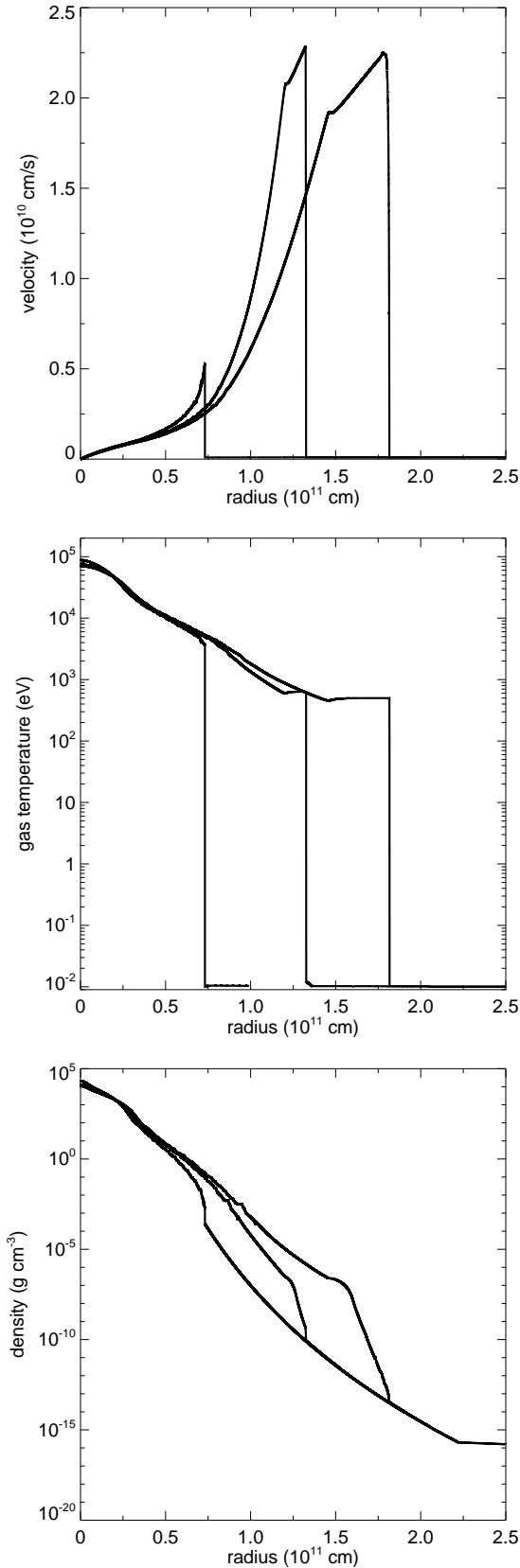


FIG. 8.— Shock breakout for the h150 PI SN in a diffuse envelope. Top: velocities; center: temperatures; bottom: densities. From left to right the times are 2.65 s, 5.12 s, 6.18 s, and 7.79 s.

not be approximated by simply stripping the H envelope from a Pop III star and then exploding it. The effects of metallicity on the evolution of the star and its ambient medium be taken into account to properly identify these events in the local universe.

We emphasize that because only a small subset of the PI SNe that are possible have been studied to date, it is premature to dismiss them as candidates for a few recent superluminous SNe (SLSNe) just because their light curves do not match those of Pop III explosions (e.g., Nicholl et al. 2013). For example, we have not examined $Z \sim 0.1 Z_{\odot}$ PI SNe crashing into dense shells ejected by the star prior to its death. Similar but less energetic Type IIn events have been found to have rapid rise times consistent with SLSNe (Whalen et al. 2013b). Had the progenitors of the PI SNe in this study ejected massive shells at later times that were within reach of their ejecta, they might have had light curves that are consistent with the superluminous events in Nicholl et al. (2013), and they may have been observable at much higher redshifts than the explosions in this paper. Such collisions are now being studied with RAGE. The large number of possibilities for PI SN progenitor structure and envelope also highlights the difficulty of matching any one PI SN candidate to current models (see also Bayless et al. 2013).

Our weak pair-instability supernovae, in which much of the ^{56}Ni falls back, produce dim, short-duration outbursts. A growing list of dim supernovae have been observed, often being classified as thermonuclear flashes on white dwarfs, the so-called “.Ia supernovae” because they are 1/10th the strength of normal supernovae (e.g., Drout et al. 2013). Many of these events have been explained as CC SNe (Fryer et al. 2007b, 2009; Moriya et al. 2010; Kleiser & Kasen 2013). But our models show that some PI SNe could also be masquerading as dim supernovae. If PI SNe can explain both superluminous and dim supernovae, it is possible that, under the right conditions (explosion energy and circumstellar medium), they could be hidden in a wide variety of supernova classes.

The effect of rotation on the light curves of PI SNe is not yet known. Yoon et al. (2012), Chatzopoulos & Wheeler (2012), and Chatzopoulos et al. (2013) find that Pop III stars that rotate at 50% of the breakup velocity at their equator can lose mass and explode as PI SNe at 85 - 135 M_{\odot} . They, like the stars in this paper, die as bare He cores, and may also explode in dense winds or shells. But even though their explosion energies and breakout radii are similar to those here, their luminosities must still be verified by simulation because they are crucially dependent on the structures of their ejecta, which are distinct from those studied here. These simulations are now in progress.

Our models demonstrate, for the first time, that some PI SNe do create massive black holes, like the 90 M_{\odot} remnant created in the h500s0 explosion. They also reveal that fallback can strongly affect the luminosity of the SN because any ^{56}Ni the explosion creates is swallowed up by the black hole at early times and therefore cannot power the light curve at later times. The creation of a black hole also admits the possibility of the formation of a black hole accretion disk system, if the core of the star has sufficient angular momentum. Because in

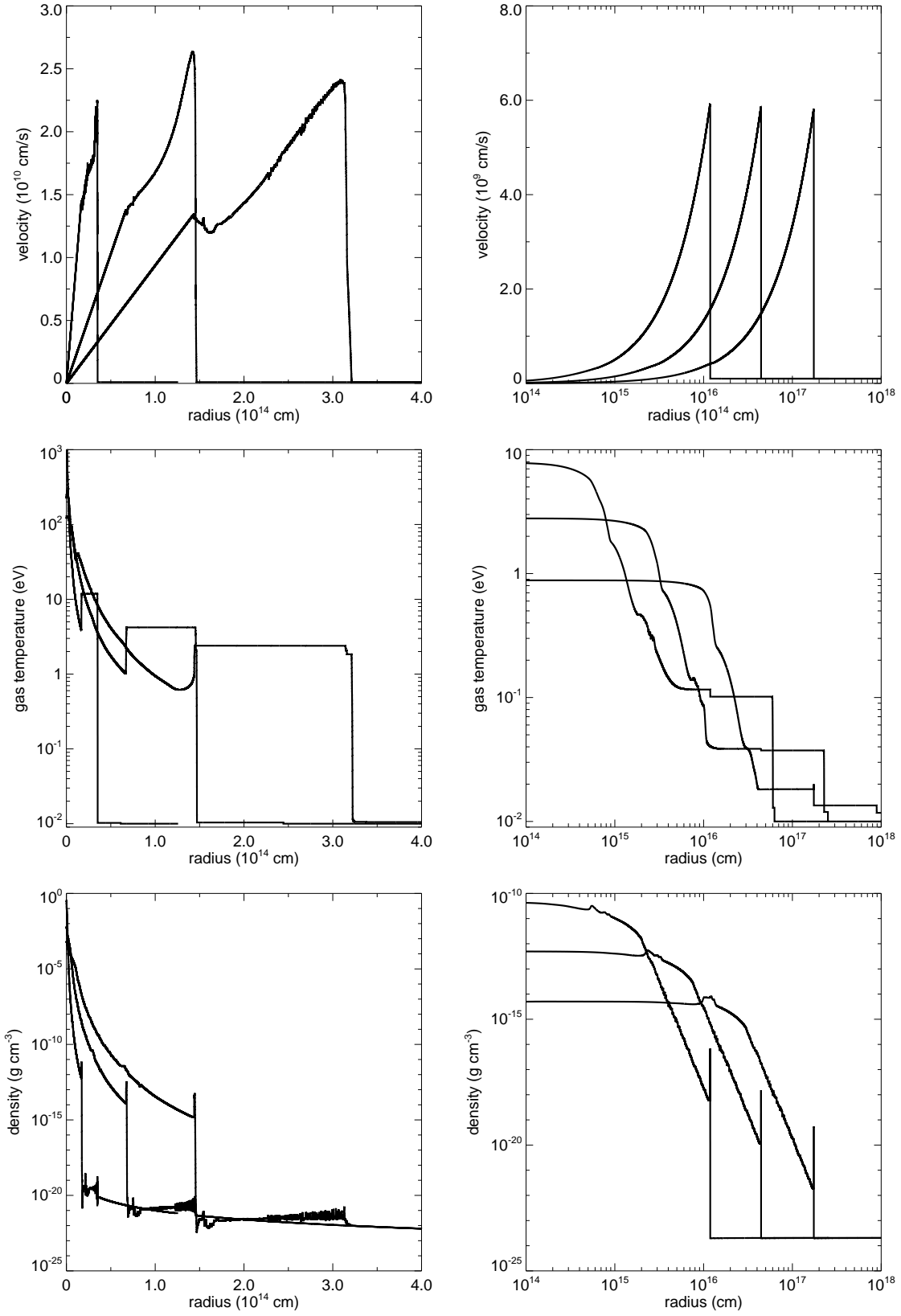


FIG. 9.— Early (left) and late (right) evolution of the h150 PI SN in a diffuse wind. Left: from left to right the times are 1164 s, 4866 s and 1.07e4 s. Right: from left to right the times are 23.0 d, 87.4 d and 346 d.

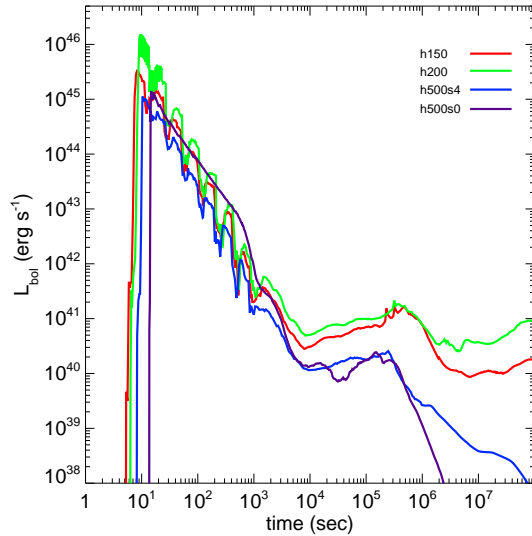


FIG. 10.— Bolometric luminosities for all 4 explosions in diffuse envelopes.

excess of $1 M_{\odot}$ can fall into the black hole every second, a small fraction of these events could be accompanied by GRBs (Whalen et al. 2008a; Mesler et al. 2013) because the star has shed its H envelope and the jet can escape.

The SN factories may ultimately discover many PI SNe, even though they can only detect them at $z \lesssim 1$, because cosmic star formation rates are so much higher at low redshifts than at high redshifts (Tornatore et al. 2007; Trenti & Stiavelli

2009; Ishida et al. 2011; Campisi et al. 2011; Robertson & Ellis 2012; Cooke et al. 2012; Wise et al. 2012; Johnson et al. 2013a; Pawlik et al. 2013; Xu et al. 2013; Hasegawa & Semelin 2013; Muratov et al. 2013). These facilities, together with future NIR observatories, will soon probe the stellar populations of both early and mature galaxies with these energetic transients.

DW was supported by the Baden-Württemberg-Stiftung by contract research via the programme Internationale Spitzenforschung II (grant P-LS-SPII/18). Both he and CJ are grateful for support by the DOE Institute for Nuclear Theory during the Extreme Computing Workshop INT-11-2a, where some of this work was performed. He also thanks Terrance Strother for running some of the models. RH was supported by the World Premier International Research Center Initiative (WPI Initiative), MEXT, Japan. NY acknowledges support from the Ministry of Higher Education and University of Malaya under the Higher Education Academic Training Scheme and the Commonwealth Scholarship Commission for the Split-Site PhD 2010 - 2011 programme at the University of Keele. AH and KC were funded by the US Department of Energy under contracts DE-FC02-01ER41176, FC02-09ER41618 (SciDAC), and DE-FG02-87ER40328. Work at LANL was done under the auspices of the National Nuclear Security Administration of the U.S. Dept of Energy at Los Alamos National Laboratory under Contract No. DE-AC52-06NA25396. All RAGE and SPECTRUM calculations were performed on Institutional Computing (IC) platforms at LANL (Mustang, Pinto and Lobo).

REFERENCES

- Abel, T., Wise, J. H., & Bryan, G. L. 2007, *ApJ*, 659, L87
- Almgren, A. S., Beckner, V. E., Bell, J. B., Day, M. S., Howell, L. H., Joggerst, C. C., Lijewski, M. J., Nonaka, A., Singer, M., & Zingale, M. 2010, *ApJ*, 715, 1221
- Alvarez, M. A., Bromm, V., & Shapiro, P. R. 2006, *ApJ*, 639, 621
- Bayless, A., Even, W., Frey, L. H., Fryer, C. L., Roming, P. R., & Young, P. A. 2013, *ApJ*, in prep
- Bromm, V., Yoshida, N., & Hernquist, L. 2003, *ApJ*, 596, L135
- Campisi, M. A., Maio, U., Salvaterra, R., & Ciardi, B. 2011, *MNRAS*, 416, 2760
- Chatzopoulos, E. & Wheeler, J. C. 2012, *ApJ*, 748, 42
- Chatzopoulos, E., Wheeler, J. C., & Couch, S. M. 2013, *ApJ*, 776, 129
- Chen, K.-J., Heger, A., & Almgren, A. S. 2011, *Computer Physics Communications*, 182, 254
- Chevalier, R. A. & Imamura, J. N. 1982, *ApJ*, 261, 543
- Cooke, J., Sullivan, M., Gal-Yam, A., Barton, E. J., Carlberg, R. G., Ryan-Weber, E. V., Horst, C., Omori, Y., & Díaz, C. G. 2012, *Nature*, 491, 228
- Crowther, P. A., Schnurr, O., Hirschi, R., Yusof, N., Parker, R. J., Goodwin, S. P., & Kassim, H. A. 2010, *MNRAS*, 408, 731
- de Souza, R. S., Ishida, E. E. O., Johnson, J. L., Whalen, D. J., & Mesinger, A. 2013, *MNRAS*, 436, 1555
- de Souza, R. S., Rodrigues, L. F. S., Ishida, E. E. O., & Opher, R. 2011, *MNRAS*, 415, 2969
- Drout, M. R., Soderberg, A. M., Mazzali, P. A., Parrent, J. T., Margutti, R., Milisavljevic, D., Sanders, N. E., Chornock, R., Foley, R. J., Kirshner, R. P., Filippenko, A. V., Li, W., Brown, P. J., Cenko, S. B., Chakraborti, S., Challis, P., Friedman, A., Ganeshalingam, M., Hicken, M., Jensen, C., Modjaz, M., Perets, H. B., Silverman, J. M., & Wong, D. S. 2013, *ApJ*, 774, 58
- Eggenberger, P., Meynet, G., Maeder, A., Hirschi, R., Charbonnel, C., Talon, S., & Ekström, S. 2008, *Ap&SS*, 316, 43
- Frey, L. H., Even, W., Whalen, D. J., Fryer, C. L., Hungerford, A. L., Fontes, C. J., & Colgan, J. 2013, *ApJS*, 204, 16
- Fryer, C. L. 1999, *ApJ*, 522, 413
- Fryer, C. L., Belczynski, K., Wiktorowicz, G., Dominik, M., Kalogera, V., & Holz, D. E. 2012, *ApJ*, 749, 91
- Fryer, C. L., Brown, P. J., Bufano, F., Dahl, J. A., Fontes, C. J., Frey, L. H., Holland, S. T., Hungerford, A. L., Immler, S., Mazzali, P., Milne, P. A., Scannapieco, E., Weinberg, N., & Young, P. A. 2009, *ApJ*, 707, 193
- Fryer, C. L., Hungerford, A. L., & Rockefeller, G. 2007a, *International Journal of Modern Physics D*, 16, 941
- Fryer, C. L., Hungerford, A. L., & Young, P. A. 2007b, *ApJ*, 662, L55
- Fryer, C. L., Whalen, D. J., & Frey, L. 2010, in *American Institute of Physics Conference Series*, Vol. 1294, American Institute of Physics Conference Series, ed. D. J. Whalen, V. Bromm, & N. Yoshida, 70–75
- Gal-Yam, A., Mazzali, P., Ofek, E. O., Nugent, P. E., Kulkarni, S. R., Kasliwal, M. M., Quimby, R. M., Filippenko, A. V., Cenko, S. B., Chornock, R., Waldman, R., Kasen, D., Sullivan, M., Beshore, E. C., Drake, A. J., Thomas, R. C., Bloom, J. S., Poznanski, D., Miller, A. A., Foley, R. J., Silverman, J. M., Arcavi, I., Ellis, R. S., & Deng, J. 2009, *Nature*, 462, 624
- Gittings, M., Weaver, R., Clover, M., Betlach, T., Byrne, N., Coker, R., Dendy, E., Hueckstaedt, R., New, K., Oakes, W. R., Ranta, D., & Stefan, R. 2008, *Computational Science and Discovery*, 1, 015005
- Glover, S. 2013, in *Astrophysics and Space Science Library*, Vol. 396, *Astrophysics and Space Science Library*, ed. T. Wiklund, B. Mobasher, & V. Bromm, 103
- Hasegawa, K. & Semelin, B. 2013, *MNRAS*, 428, 154
- Heger, A. & Woosley, S. E. 2002, *ApJ*, 567, 532
- Hirschi, R., Meynet, G., & Maeder, A. 2004, *A&A*, 425, 649
- Imamura, J. N., Wolff, M. T., & Durisen, R. H. 1984, *ApJ*, 276, 667

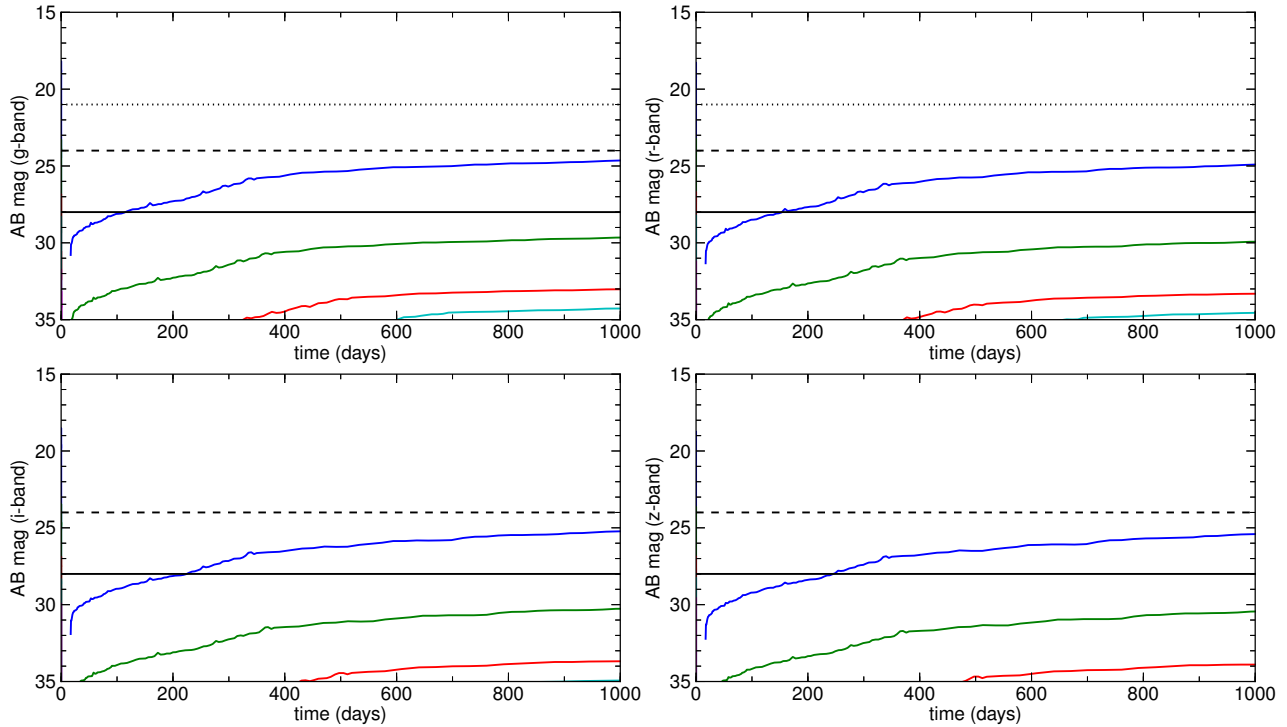


FIG. 11.— Light curves for the h150 PI SN at $z = 0.01$ (blue), $z = 0.1$ (green), $z = 0.5$ (red), $z = 1$ (teal), and $z = 2$ (purple). Dotted line: PTF detection limit; dashed line: Pan-STARRS detection limit; solid line: LSST detection limit.

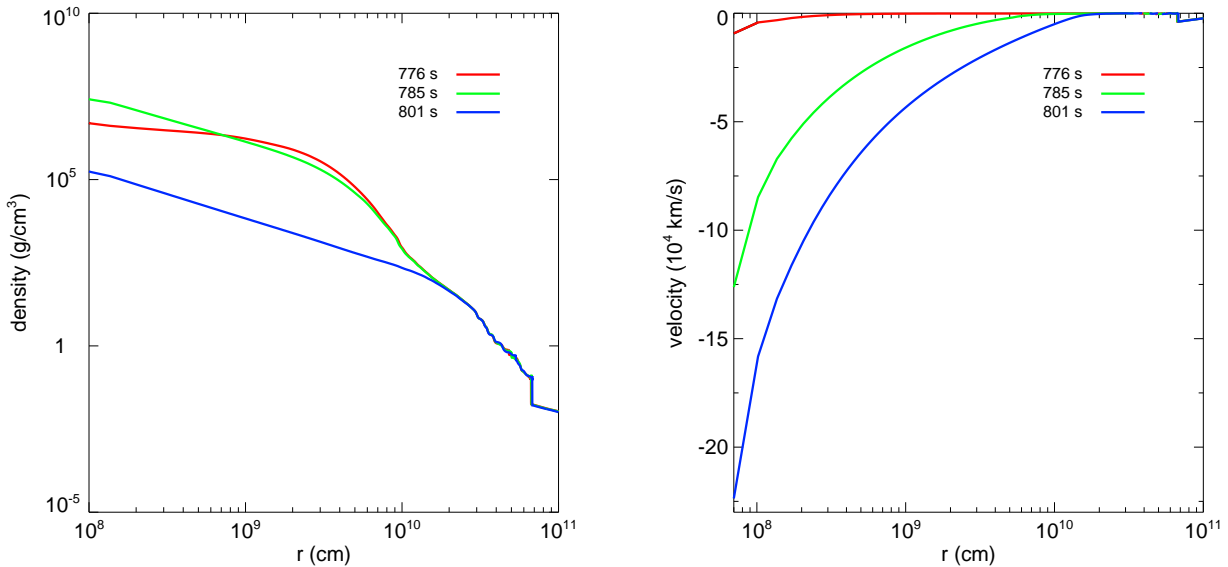


FIG. 12.—Fallback in the h500s0 explosion. Left: densities. Right: velocities.

Ishida, E. E. O., de Souza, R. S., & Ferrara, A. 2011, MNRAS, 418, 500

Ivezic, Z., Tyson, J. A., Acosta, E., Allsman, R., Anderson, S. F., Andrew, J., Angel, R., Axelrod, T., Barr, J. D., Becker, A. C., Becla, J., Beldica, C., Blandford, R. D., Bloom, J. S., Borne, K., Brandt, W. N., Brown, M. E., Bullock, J. S., Burke, D. L., Chandrasekharan, S., Chesley, S., Claver, C. F., Connolly, A., Cook, K. H., Cooray, A., Covey, K. R., Cribbs, C., Cutri, R., Daues, G., Delgado, F., Ferguson, H., Gawiser, E., Geary, J. C., Gee, P., Geha, M., Gibson, R. R., Gilmore, D. K., Gressler, W. J., Hogan, C., Huffer, M. E., Jacoby, S. H., Jain, B., Jernigan, J. G., Jones, R. L., Juric, M., Kahn, S. M., Kalirai, J. S., Kantor, J. P., Kessler, R., Kirkby, D., Knox, L., Krabbendam, V. L., Krughoff, S., Kulkarni, S., Lambert, R., Levine, D., Liang, M., Lim, K., Lupton, R. H., Marshall, P., Marshall, S., May, M., Miller, M., Mills, D. J., Monet, D. G., Neill, D. R., Nordby, M., O'Connor, P., Oliver, J., Olivier, S. S., Olsen, K., Owen, R. E., Peterson, J. R., Petry, C. E., Pierfederici, F., Pietrowicz, S., Pike, R., Pinto, P. A., Plante, R., Radeka, V., Rasmussen, A., Ridgway, S. T., Rosing, W., Saha, A., Schalk, T. L., Schindler, R. H., Schneider, D. P., Schumacher, G., Sebag, J., Seppala, L. G., Shipsey, I., Silvestri,

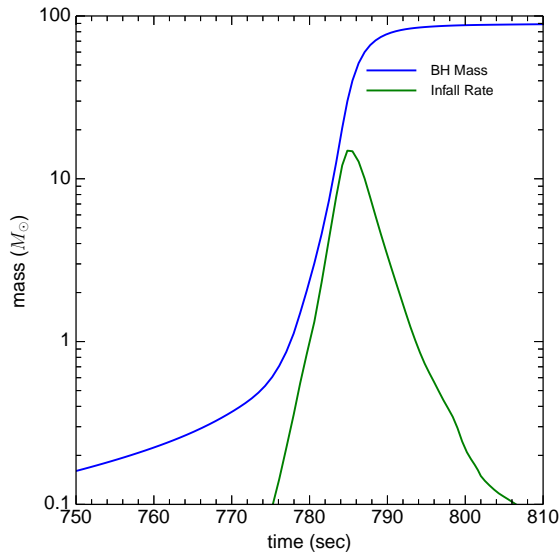


FIG. 13.— Central black hole mass and infall rates in the h500s0 PI SN.

- Joggerst, C. C., Almgren, A., Bell, J., Heger, A., Whalen, D., & Woosley, S. E. 2010, *ApJ*, 709, 11
- Joggerst, C. C. & Whalen, D. J. 2011, *ApJ*, 728, 129
- Johnson, J. L., Dalla, V. C., & Khochfar, S. 2013a, *MNRAS*, 428, 1857
- Johnson, J. L., Whalen, D. J., Even, W., Fryer, C. L., Heger, A., Smidt, J., & Chen, K.-J. 2013b, *arXiv:1304.4601*
- Kaiser, N., Aussel, H., Burke, B. E., Boesgaard, H., Chambers, K., Chun, M. R., Heasley, J. N., Hodapp, K.-W., Hunt, B., Jedicke, R., Jewitt, D., Kudritzki, R., Luppino, G. A., Maberry, M., Magnier, E., Monet, D. G., Onaka, P. M., Pickles, A. J., Rhoads, P. H. H., Simon, T., Szalay, A., Szapudi, I., Tholen, D. J., Tonry, J. L., Waterson, M., & Wick, J. 2002, in *Society of Photo-Optical Instrumentation Engineers (SPIE) Conference Series*, Vol. 4836, Society of Photo-Optical Instrumentation Engineers (SPIE) Conference Series, ed. J. A. Tyson & S. Wolff, 154–164
- Kasen, D., Woosley, S. E., & Heger, A. 2011, *ApJ*, 734, 102
- Kitayama, T. & Yoshida, N. 2005, *ApJ*, 630, 675
- Kitayama, T., Yoshida, N., Susa, H., & Umemura, M. 2004, *ApJ*, 613, 631
- Kleiser, I. & Kasen, D. 2013, *arXiv:1309.4088*
- Law, N. M., Kulkarni, S. R., Dekany, R. G., Ofek, E. O., Quimby, R. M., Nugent, P. E., Surace, J., Grillmair, C. C., Bloom, J. S., Kasliwal, M. M., Bildsten, L., Brown, T., Cenko, S. B., Ciardi, D., Croner, E., Djorgovski, S. G., van Eyken, J., Filippenko, A. V., Fox, D. B., Gal-Yam, A., Hale, D., Hamam, N., Helou, G., Henning, J., Howell, D. A., Jacobsen, J., Laher, R., Mattingly, S., McKenna, D., Pickles, A., Poznanski, D., Rahmer, G., Rau, A., Rosing, W., Shara, M., Smith, R., Starr, D., Sullivan, M., Velur, V., Walters, R., & Zolkower, J. 2009, *PASP*, 121, 1395
- Madau, P. 1995, *ApJ*, 441, 18
- Maeder, A. 2009, *Physics, Formation and Evolution of Rotating Stars* (Springer Berlin Heidelberg)
- Magee, N. H., Abdallah, Jr., J., Clark, R. E. H., Cohen, J. S., Collins, L. A., Csanak, G., Fontes, C. J., Gauger, A., Keady, J. J., Kilcrease, D. P., & Merts, A. L. 1995, in *Astronomical Society of the Pacific Conference Series*, Vol. 78, *Astrophysical Applications of Powerful New Databases*, ed. S. J. Adelman & W. L. Wiese, 51
- Meiksin, A. & Whalen, D. J. 2013, *MNRAS*, 430, 2854
- Mesler, R. A., Whalen, D. J., Lloyd-Ronning, N. M., Fryer, C. L., & Pihlström, Y. M. 2012, *ApJ*, 757, 117
- , 2013, *ApJ*, in prep
- Mokiem, M. R., de Koter, A., Vink, J. S., Puls, J., Evans, C. J., Smartt, S. J., Crowther, P. A., Herrero, A., Langer, N., Lennon, D. J., Najarro, F., & Villamariz, M. R. 2007, *A&A*, 473, 603
- Moriya, T., Tominaga, N., Tanaka, M., Nomoto, K., Sauer, D. N., Mazzali, P. A., Maeda, K., & Suzuki, T. 2010, *ApJ*, 719, 1445
- Muratov, A. L., Gnedin, O. Y., Gnedin, N. Y., & Zemp, M. 2013, *ApJ*, 773, 19
- Nicholl, M., Smartt, S. J., Jerkstrand, A., Inserra, C., McCrum, M., Kotak, R., Fraser, M., Wright, D., Chen, T.-W., Smith, K., Young, D. R., Sim, S. A., Valenti, S., Howell, D. A., Bresolin, F., Kudritzki, R. P., Tonry, J. L., Huber, M. E., Rest, A., Pastorello, A., Tomasella, L., Cappellaro, E., Benetti, S., Mattila, S., Kankare, E., Kangas, T., Leloudas, G., Sollerman, J., Taddia, F., Berger, E., Chornock, R., Narayan, G., Stubbs, C. W., Foley, R. J., Lunnan, R., Soderberg, A., Sanders, N., Milisavljevic, D., Margutti, R., Kirshner, R. P., Elias-Rosa, N., Morales-Garoffolo, A., Taubenberger, S., Botticella, M. T., Gezari, S., Urata, Y., Rodney, S., Riess, A. G., Scolnic, D., Wood-Vasey, W. M., Burgett, W. S., Chambers, K., Flewelling, H. A., Magnier, E. A., Kaiser, N., Metcalfe, N., Morgan, J., Price, P. A., Sweeney, W., & Waters, C. 2013, *Nature*, 502, 346
- Nugis, T. & Lamers, H. J. G. L. M. 2000, *A&A*, 360, 227
- Pan, T., Kasen, D., & Loeb, A. 2012a, *MNRAS*, 422, 2701
- Pan, T., Loeb, A., & Kasen, D. 2012b, *MNRAS*, 423, 2203
- Pawlik, A. H., Milosavljević, M., & Bromm, V. 2013, *ApJ*, 767, 59
- Popham, R., Woosley, S. E., & Fryer, C. 1999, *ApJ*, 518, 356
- Robertson, B. E. & Ellis, R. S. 2012, *ApJ*, 744, 95
- Scannapieco, E., Madau, P., Woosley, S., Heger, A., & Ferrara, A. 2005, *ApJ*, 633, 1031
- Schaerer, D. 2002, *A&A*, 382, 28
- Su, J., Stiavelli, M., Oesch, P., Trenti, M., Bergeron, E., Bradley, L., Carollo, M., Dahlen, T., Ferguson, H. C., Giallisco, M., Koekemoer, A., Lilly, S., Lucas, R. A., Mobasher, B., Panagia, N., & Pavlovsky, C. 2011, *ApJ*, 738, 123
- Tornatore, L., Ferrara, A., & Schneider, R. 2007, *MNRAS*, 382, 945
- Trenti, M. & Stiavelli, M. 2009, *ApJ*, 694, 879
- Vasiliev, E. O., Vorobyov, E. I., Matvienko, E. E., Razoumov, A. O., & Shchekinov, Y. A. 2012, *Astronomy Reports*, 56, 895
- Vink, J. S., de Koter, A., & Lamers, H. J. G. L. M. 2001, *A&A*, 369, 574
- Weaver, T. A., Zimmerman, G. B., & Woosley, S. E. 1978, *ApJ*, 225, 1021
- Whalen, D., Abel, T., & Norman, M. L. 2004, *ApJ*, 610, 14
- Whalen, D. & Norman, M. L. 2006, *ApJS*, 162, 281
- , 2008a, *ApJ*, 673, 664
- Whalen, D., Prochaska, J. X., Heger, A., & Tumlinson, J. 2008a, *ApJ*, 682, 1114
- Whalen, D., van Veelen, B., O’Shea, B. W., & Norman, M. L. 2008b, *ApJ*, 682, 49
- Whalen, D. J. 2012, *arXiv:1209.4688*
- Whalen, D. J., Even, W., Frey, L. H., Smidt, J., Johnson, J. L., Lovekin, C. C., Fryer, C. L., Stiavelli, M., Holz, D. E., Heger, A., Woosley, S. E., & Hungerford, A. L. 2013a, *ApJ*, 777, 110
- Whalen, D. J., Even, W., Lovekin, C. C., Fryer, C. L., Stiavelli, M., Roming, P. W. A., Cooke, J., Pritchard, T. A., Holz, D. E., & Knight, C. 2013b, *ApJ*, 768, 195
- Whalen, D. J., Even, W., Smidt, J., Heger, A., Chen, K.-J., Fryer, C. L., Stiavelli, M., Xu, H., & Joggerst, C. C. 2013c, *ApJ*, 778, 17
- Whalen, D. J. & Fryer, C. L. 2012, *ApJ*, 756, L19
- Whalen, D. J., Fryer, C. L., Holz, D. E., Heger, A., Woosley, S. E., Stiavelli, M., Even, W., & Frey, L. H. 2013d, *ApJ*, 762, L6
- Whalen, D. J., Joggerst, C. C., Fryer, C. L., Stiavelli, M., Heger, A., & Holz, D. E. 2013e, *ApJ*, 768, 95
- Whalen, D. J., Johnson, J. L., Smidt, J., Heger, A., Even, W., & Fryer, C. L. 2013f, *ApJ*, 777, 99
- Whalen, D. J., Johnson, J. L., Smidt, J., Meiksin, A., Heger, A., Even, W., & Fryer, C. L. 2013g, *ApJ*, 774, 64
- Whalen, D. J. & Norman, M. L. 2008b, *ApJ*, 672, 287
- Wise, J. H. & Abel, T. 2008, *ApJ*, 684, 1
- Wise, J. H., Turk, M. J., Norman, M. L., & Abel, T. 2012, *ApJ*, 745, 50
- Woosley, S. E., Heger, A., & Weaver, T. A. 2002, *Reviews of Modern Physics*, 74, 1015
- Xu, H., Wise, J. H., & Norman, M. L. 2013, *ApJ*, 773, 83
- Yoon, S.-C., Dierks, A., & Langer, N. 2012, *A&A*, 542, A113

Young, D. R., Smartt, S. J., Valenti, S., Pastorello, A., Benetti, S., Benn, C. R., Bersier, D., Botticella, M. T., Corradi, R. L. M., Harutyunyan, A. H., Hrudkova, M., Hunter, I., Mattila, S., de Mooij, E. J. W., Navasardyan, H., Snellen, I. A. G., Tanvir, N. R., & Zampieri, L. 2010, *A&A*, 512, A70+
Yusof, N., Hirschi, R., Meynet, G., Crowther, P. A., Ekström, S., Frischknecht, U., Georgy, C., Abu Kassim, H., & Schnurr, O. 2013, *MNRAS*, 433, 1114